

Nonisothermal crystallization kinetics, fragility and thermodynamics of $Ti_{20}Zr_{20}Cu_{20}Ni_{20}Be_{20}$ high entropy bulk metallic glass

Pan Gong,^{a)} Shaofan Zhao, Hongyu Ding, and Kefu Yao^{b)}

School of Materials Science and Engineering, Tsinghua University, Beijing 100084, China

Xin Wang

School of Materials Science and Engineering, Hebei University of Technology, Hongqiao District, Tianjin 300130, China

(Received 1 May 2015; accepted 3 August 2015)

The nonisothermal crystallization kinetics, fragility, and thermodynamics of $Ti_{20}Zr_{20}Cu_{20}Ni_{20}Be_{20}$ high entropy bulk metallic glass (HE-BMG) have been investigated by differential scanning calorimetry. The activation energies for the glass transition and crystallization events were determined by Kissinger and Ozawa methods. The value of local Avrami exponent is less than 1.5 in most cases for all the three crystallization events, indicating that the major crystallization mechanism is diffusion-controlled growth of pre-existing nuclei. The local activation energy is stable during the whole crystallization process and this further confirms that the crystallization occurs through a single mechanism. $Ti_{20}Zr_{20}Cu_{20}Ni_{20}Be_{20}$ alloy can be classified into “strong glass formers” according to the estimated fragility index and also shows a relatively low value of Gibbs free energy difference. However, compared with $Zr_{41.2}Ti_{13.8}Cu_{12.5}Ni_{10}Be_{22.5}$ BMG, the glass-forming ability of $Ti_{20}Zr_{20}Cu_{20}Ni_{20}Be_{20}$ HE-BMG is much lower and the related reasons have been discussed.

I. INTRODUCTION

High entropy alloys (HEAs)^{1–3} and bulk metallic glasses (BMGs)^{4,5} are both potential candidate materials for industrial application. Because of the high entropy effect, HEAs always form simple solid solutions with face-centered cubic (FCC) and/or body-centered cubic (BCC) structures rather than intermetallic compounds. However, as the “confusion principle” is a necessary condition for glass formation, some HEAs can also form amorphous structure.^{6,7} As a combination of HEAs and BMGs, the bulk metallic glassy alloys which consist of at least five principal elements in equimolar or near-equimolar ratios have been defined as high entropy metallic glasses.^{8,9}

As HE-BMG is a new research topic, only a few HE-BMGs, such as $Ti_{20}Zr_{20}Hf_{20}Cu_{20}Ni_{20}$,¹⁰ $Sr_{20}Ca_{20}Yb_{20}Mg_{20}Zn_{20}$,¹¹ $Zn_{20}Ca_{20}Sr_{20}Yb_{20}(Li_{0.55}Mg_{0.45})_{20}$,⁸ and $Pd_{20}Pt_{20}Cu_{20}Ni_{20}P_{20}$,¹² have been developed and the glass-forming ability of most developed HE-BMGs is relatively low. So it is meaningful to develop an effective way for composition design of novel HE-BMGs with good glass-forming ability. In our previous study,¹³ a way for designing high entropy bulk glassy alloy has been proposed that HE-BMG can be

derived from the existing BMG system with superior glass-forming ability (GFA). It is well known that many Zr–Ti–Cu–Ni–Be or Ti–Zr–Cu–Ni–Be quinary alloys possess superior glass-forming ability.^{14–16} In this sense, the equiatomic and near-equiatomic alloys in Ti–Zr–Cu–Ni–Be system are probably good glass formers. Based on the above conception, a $Ti_{20}Zr_{20}Cu_{20}Ni_{20}Be_{20}$ HE-BMG with a critical size of 3 mm has been successfully developed.¹³ Compared with other glass forming alloys in the same system, the glass-forming ability of $Ti_{20}Zr_{20}Cu_{20}Ni_{20}Be_{20}$ HE-BMG is much lower.

For understanding the thermal stability and crystallization mechanism, it is meaningful to investigate the crystallization kinetics and thermodynamic properties of BMGs. Many papers have been published on the crystallization kinetics of BMGs, including Zr-based,¹⁷ Ti-based,¹⁸ Cu-based,¹⁹ Fe-based,²⁰ Mg-based,²¹ Ni-based,²² Ca-based,²³ Al-based,²⁴ and Ce-based BMGs,²⁵ etc. However, very little information is available to date for HE-BMGs. In this study, the nonisothermal kinetics, kinetic fragility, and thermodynamic characteristics of $Ti_{20}Zr_{20}Cu_{20}Ni_{20}Be_{20}$ HE-BMG have been systematically studied by differential scanning calorimetry (DSC). $Zr_{41.2}Ti_{13.8}Cu_{12.5}Ni_{10}Be_{22.5}$ BMG, which is a typical representative of conventional BMGs with good glass-forming ability in Ti–Zr–Cu–Ni–Be quinary system, was chosen as a reference. Our research is an attempt to get a better idea of the characteristics of HE-BMGs.

Contributing Editor: Jörg Löffler

Address all correspondence to these authors.

^ae-mail: gongpan126@gmail.com

^be-mail: kfya@tsinghua.edu.cn

DOI: 10.1557/jmr.2015.253

II. EXPERIMENTAL PROCEDURE

The master ingots with a nominal composition of $Ti_{20}Zr_{20}Cu_{20}Ni_{20}Be_{20}$ were prepared by arc-melting a mixture of Ti, Zr, Cu, Ni, and Be metals (purity $\geq 99.9\%$) in a Ti-gettered high purity argon atmosphere. The ingots were flipped and re-melted several times to ensure compositional homogeneity. Cylindrical rods with a diameter of 3 mm and a length of ~ 30 mm were produced by copper mold suction casting. The as-cast 3 mm-diameter rod was sealed into a quartz tube under high vacuum and annealed at 753 and 813 K, respectively, for 1 h to find out the crystalline phases. The microstructure of the as-cast and annealed samples was examined by x-ray diffraction (XRD, Rigaku D/max-RB, Cu $K\alpha$ radiation, Tokyo, Japan). Thermal analysis was carried out in a DSC (NETZSCH 404 F1 Pegasus, Selb, Germany) under a flow of purified argon at different heating rates in the range of 5–40 K/min using alumina crucibles. The DSC system was calibrated for temperature and enthalpy using indium and zinc standards. To avoid the influence of the sample size and sample mass, all the DSC samples were cut from the same 3 mm-diameter fully amorphous rod and the weight of each sample was around 15 mg.

III. RESULTS AND DISCUSSION

A. Continuous heating

It was already known that HEAs do not always form simple solid solutions with FCC and/or BCC structures. This is entirely dependent on the chemistry of the alloy and the topology/atomic size differences of the alloy constituents. Based on the solid-solution phase formation rules for multicomponent alloys proposed by Zhang et al.,⁷ $Ti_{20}Zr_{20}Cu_{20}Ni_{20}Be_{20}$ alloy is located in the BMG forming zone. Our previous study shows that $Ti_{20}Zr_{20}Cu_{20}Ni_{20}Be_{20}$ alloy is a bulk glass former with a critical size of 3 mm.¹³ Correspondingly, as shown in Fig. 1, the XRD pattern of as-cast 3 mm-diameter $Ti_{20}Zr_{20}Cu_{20}Ni_{20}Be_{20}$ alloy rod consists of only a broad halo and no other sharp peaks corresponding to crystalline phases can be observed, indicating that the alloy rod possesses fully amorphous structure.

Figure 2 shows the typical nonisothermal DSC curves of the $Ti_{20}Zr_{20}Cu_{20}Ni_{20}Be_{20}$ HE-BMG obtained at various heating rates of 5, 10, 20, and 40 K/min. All the DSC traces exhibit an endothermic event corresponding to the glass transition followed by three exothermic crystallization peaks. The characteristic temperatures (such as the glass transition temperature T_g , the onset crystallization temperature T_x , and the peak temperatures T_{p1} , T_{p2} , and T_{p3}) and supercooled liquid region (defined as $T_x - T_g$) are listed in Table I. The crystallization of $Ti_{20}Zr_{20}Cu_{20}Ni_{20}Be_{20}$ HE-BMG is a multiple stage process and rather complex.

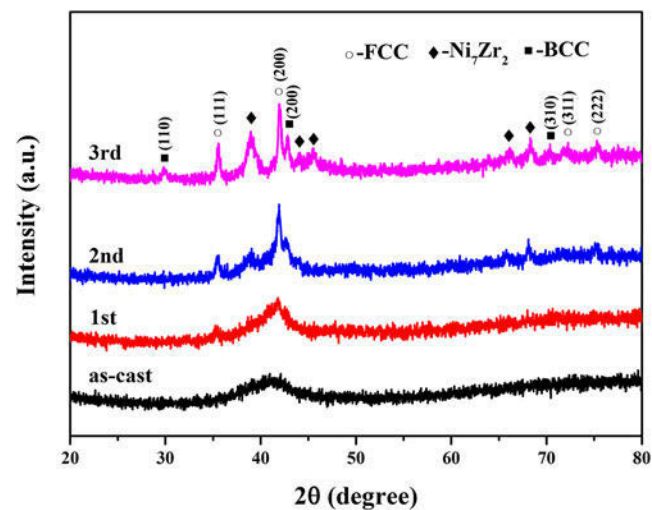


FIG. 1. XRD patterns of as-cast and annealed 3 mm-diameter $Ti_{20}Zr_{20}Cu_{20}Ni_{20}Be_{20}$ rod samples.

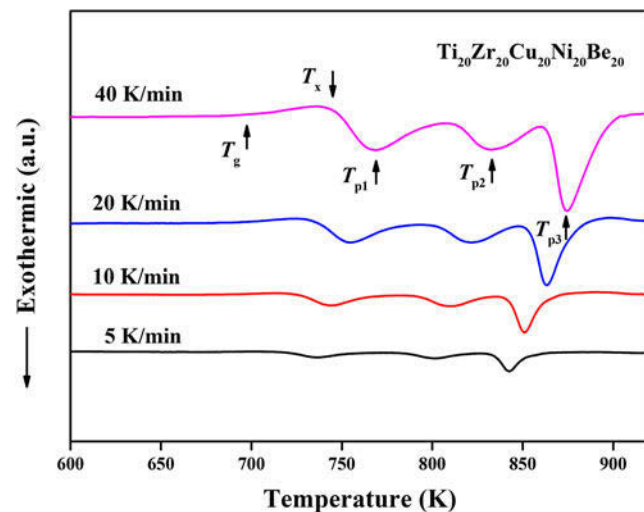


FIG. 2. Continuous DSC traces of the $Ti_{20}Zr_{20}Cu_{20}Ni_{20}Be_{20}$ HE-BMG at different heating rates.

TABLE I. The thermal properties of the $Ti_{20}Zr_{20}Cu_{20}Ni_{20}Be_{20}$ HE-BMG measured at different heating rates. The measurement errors lie within ± 1 K for the temperatures.

| Heating rate (K/min) | T_g (K) | T_x (K) | T_{p1} (K) | T_{p2} (K) | T_{p3} (K) | ΔT_x (K) |
|----------------------|-----------|-----------|--------------|--------------|--------------|------------------|
| 5 | | 671.7 | 718.4 | 737.1 | 801.2 | 842.5 |
| 10 | | 679.3 | 724.8 | 743.9 | 809.9 | 850.9 |
| 20 | | 687.1 | 735.1 | 755.2 | 821.9 | 863.3 |
| 40 | | 696.4 | 746.8 | 769.0 | 832.6 | 874.6 |
| | | | | | | 46.7 |
| | | | | | | 45.5 |
| | | | | | | 48.0 |
| | | | | | | 50.4 |

To indentify the precipitated phases underlying various crystallization stages, the 3 mm-diameter $Ti_{20}Zr_{20}Cu_{20}Ni_{20}Be_{20}$ fully glassy samples were heated in DSC furnace to selected temperatures (T_{p1} ²⁰ K/min,

$T_{\text{p}2}^{20 \text{ K/min}}$, and $T_{\text{p}3}^{20 \text{ K/min}}$) at a heating rate of 20 K/min and cooled to room temperature subsequently without holding time. XRD measurements for samples after annealing treatments at various selected temperatures were carried out. As shown in Fig. 1, the primary crystalline phase was indexed as FCC solid solution appearing at $T_{\text{p}1}^{20 \text{ K/min}}$. When the annealing temperature increases to $T_{\text{p}2}^{20 \text{ K/min}}$, two crystalline phases FCC solid solution and Ni_7Zr_2 intermetallic compound were detected. Upon heating to the third exothermic peak, BCC solid solution was observed in addition to the FCC solid solution and Ni_7Zr_2 intermetallic compound. In contrast, there have been a number of reports on Ti and/or Zr containing BMGs showing the formation of icosahedral quasicrystals or Laves type-phases during crystallization.^{26–29} This indicates that the high entropy effect does play an important role on the crystallization behavior of HE-BMGs. With the increase of heating rate, all the characteristic temperatures of $\text{Ti}_{20}\text{Zr}_{20}\text{Cu}_{20}\text{Ni}_{20}\text{Be}_{20}$ HE-BMG shift to higher temperature. This phenomenon has also been observed for other BMGs.^{17–25}

Based on the DSC data, the apparent activation energy for the glass transition and crystallization can be evaluated by the Kissinger and Ozawa equations, respectively. The Kissinger equation can be written as³⁰:

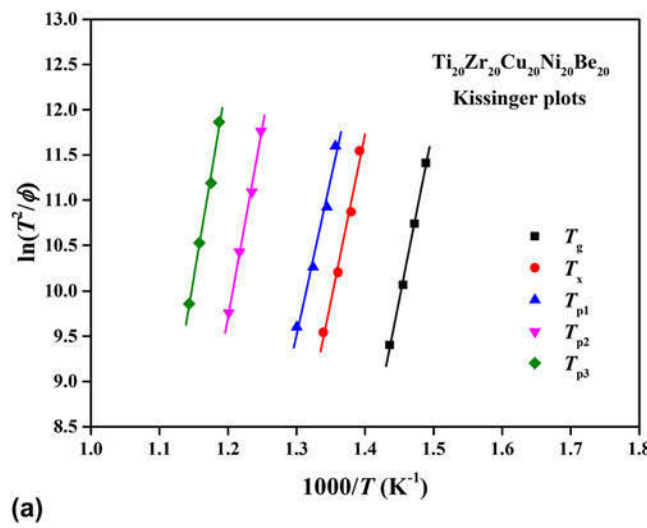


FIG. 3. (a) Kissinger plots and (b) Ozawa plots of the $\text{Ti}_{20}\text{Zr}_{20}\text{Cu}_{20}\text{Ni}_{20}\text{Be}_{20}$ HE-BMG.

TABLE II. The apparent activation energies derived with Kissinger and Ozawa methods for $\text{Ti}_{20}\text{Zr}_{20}\text{Cu}_{20}\text{Ni}_{20}\text{Be}_{20}$ HE-BMG. The activation energies of $\text{Zr}_{41.2}\text{Ti}_{13.8}\text{Cu}_{12.5}\text{Ni}_{10}\text{Be}_{22.5}$ (Vit 1) BMG obtained by Kissinger method are also listed as a Ref. 19.

| Alloy | Method | E_g (kJ/mol) | E_x (kJ/mol) | $E_{\text{p}1}$ (kJ/mol) | $E_{\text{p}2}$ (kJ/mol) | $E_{\text{p}3}$ (kJ/mol) |
|--|-----------|-----------------|------------------|--------------------------|--------------------------|--------------------------|
| $\text{Ti}_{20}\text{Zr}_{20}\text{Cu}_{20}\text{Ni}_{20}\text{Be}_{20}$ | Kissinger | 317.2 ± 8.5 | 307.0 ± 18.1 | 286.9 ± 19.6 | 347.3 ± 9.7 | 374.4 ± 13.6 |
| | Ozawa | 312.5 ± 8.5 | 303.5 ± 18.1 | 284.6 ± 19.6 | 343.0 ± 9.7 | 369.5 ± 13.6 |
| $\text{Zr}_{41.2}\text{Ti}_{13.8}\text{Cu}_{12.5}\text{Ni}_{10}\text{Be}_{22.5}$ | Kissinger | 535 ± 17 | 162 ± 6 | 203 ± 5 | 271 ± 7 | 301 ± 9 |

$$\ln\left(\frac{\phi}{T^2}\right) = -\frac{E}{RT} + b_1 \quad , \quad (1)$$

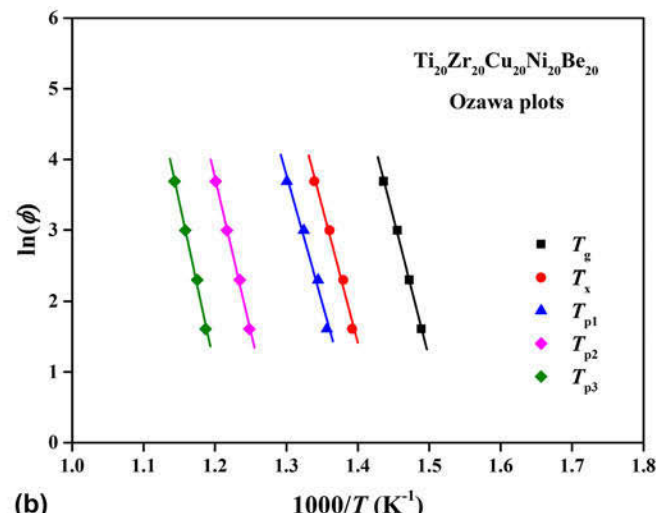
where ϕ is the heating rate, R is the gas constant (8.314 J/mol K), and b_1 is a constant. T is a specific characteristic temperature, such as T_g , T_x , $T_{\text{p}1}$, $T_{\text{p}2}$, and $T_{\text{p}3}$, while E denotes the corresponding activation energy, such as E_g , E_x , $E_{\text{p}1}$, $E_{\text{p}2}$, and $E_{\text{p}3}$.

The Ozawa equation can be expressed as³¹:

$$\ln(\phi) = -1.052 \frac{E}{RT} + b_2 \quad , \quad (2)$$

where b_2 is another constant.

The Kissinger and Ozawa plots of $\text{Ti}_{20}\text{Zr}_{20}\text{Cu}_{20}\text{Ni}_{20}\text{Be}_{20}$ HE-BMG at different heating rates are shown in Fig. 3(a) and 3(b), respectively. By linear fitting, the activation energies such as E_g , E_x , $E_{\text{p}1}$, $E_{\text{p}2}$, and $E_{\text{p}3}$ for $\text{Ti}_{20}\text{Zr}_{20}\text{Cu}_{20}\text{Ni}_{20}\text{Be}_{20}$ HE-BMG have been obtained and listed in Table II. The activation energies estimated from Kissinger and Ozawa methods are approximately equal to each other. It can be noticed that $E_{\text{p}1}$ is smaller than E_x , and this means that the grain growth process is easier to occur than the nucleation process for the first crystallization event. As $E_{\text{p}3} > E_{\text{p}2} > E_{\text{p}1}$, the sequence of the difficulty during the crystallization is the first step, the second step, and the third step.



To find the difference between HE-BMGs and conventional BMGs, the activation energies of $Zr_{41.2}Ti_{13.8}Cu_{12.5}Ni_{10}Be_{22.5}$ (Vit 1) BMG, which is a typical alloy in Zr-Ti-Cu-Ni-Be quinary alloy system with nonequal atomic concentration, are also summarized in Table II.¹⁷ By comparison, the E_g value of $Ti_{20}Zr_{20}Cu_{20}Ni_{20}Be_{20}$ HE-BMG is smaller than that of $Zr_{41.2}Ti_{13.8}Cu_{12.5}Ni_{10}Be_{22.5}$ alloy, indicating that $Ti_{20}Zr_{20}Cu_{20}Ni_{20}Be_{20}$ HE-BMG possesses less stable glassy structure.³² Moreover, the relatively large value of E_x means $Ti_{20}Zr_{20}Cu_{20}Ni_{20}Be_{20}$ HE-BMG has a good stability in thermodynamics.

B. Nonisothermal crystallization kinetics

Figure 4 shows the crystallized volume fraction x of the first, second, and third exothermic peak for $Ti_{20}Zr_{20}Cu_{20}Ni_{20}Be_{20}$ HE-BMG with a dependence of

temperature T at different heating rates. All the curves exhibit a sigmoid shape, indicating that the crystallization rate is slower at the beginning and end of the crystallization process.

As the nucleation and growth always do not remain the same way during the whole crystallization process, the local Avrami exponent $n(x)$ was used to study the crystallization mechanism of $Ti_{20}Zr_{20}Cu_{20}Ni_{20}Be_{20}$ HE-BMG. In case of isothermal process, $n(x)$ can be given as follows based on Johnson-Mehl-Avrami (JMA) equation³³:

$$n(x) = \frac{d \ln[-\ln(1-x)]}{d \ln(t - t_0)} , \quad (3)$$

where x is the crystallized volume fraction, t is the time corresponding to the crystallized volume fraction, and t_0 is the incubation time for nucleation.

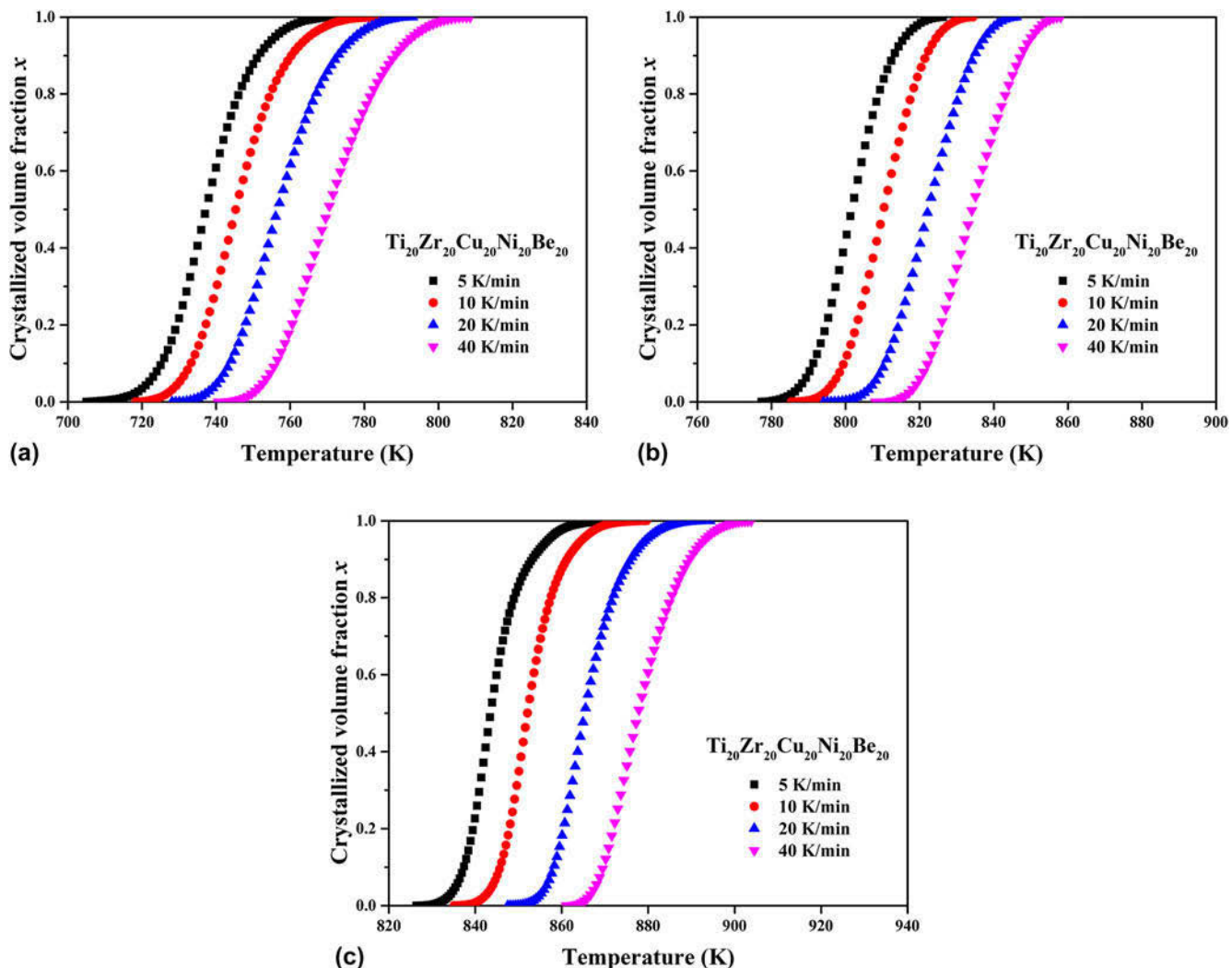


FIG. 4. Plots of crystallized volume fraction x versus temperature T of the $Ti_{20}Zr_{20}Cu_{20}Ni_{20}Be_{20}$ HE-BMG at different heating rates for the (a) first, (b) second, and (c) third crystallization events.

Blazquez et al.³⁴ extends the JMA equation to non-isothermal process under the approximation of iso-kinetic behavior, which gives the relation:

$$n(x) = \frac{1}{1 + (E_a/RT)(1 - T/T_0)} \cdot \frac{d \ln[-\ln(1 - x)]}{d \ln[(T - T_0)/\phi]} , \quad (4)$$

where T_0 is the onset temperature of crystallization for each exothermic peak and E_a is the activation energy.

Figure 5 shows the plots of $\ln[-\ln(1 - x)]$ versus $\ln[(T - T_0)/\phi]$ of $Ti_{20}Zr_{20}Cu_{20}Ni_{20}Be_{20}$ HE-BMG. Based on the JMA curves in Fig. 5 and Eq. (4), the local Avrami exponent $n(x)$ of the first, second, and third crystallization events can be obtained and shown in Figs. 6(a)–6(c), respectively.

The Avrami exponent can be expressed as³⁵:

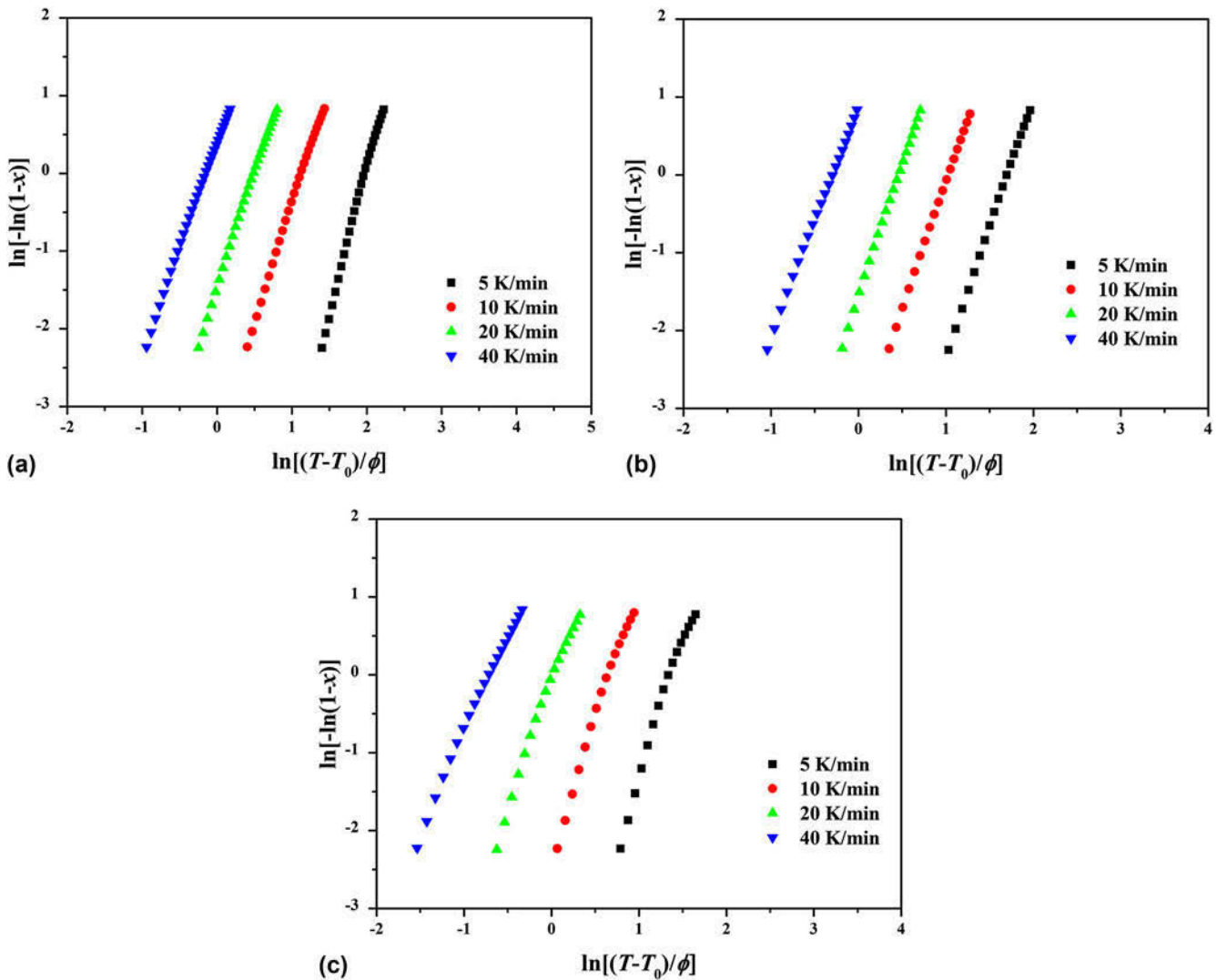


FIG. 5. JMA plots of the $Ti_{20}Zr_{20}Cu_{20}Ni_{20}Be_{20}$ HE-BMG at different heating rates for the (a) first, (b) second, and (c) third crystallization events.

$$n = a + bc \quad , \quad (5)$$

where a is the nucleation index ($a = 0$ for zero nucleation rate; $0 < a < 1$ for decreasing nucleation rate; $a = 1$ for constant nucleation rate and $a > 1$ for increasing nucleation rate), b is the dimensionality of the growth ($b = 1, 2$, and 3 for one-, two-, and three-dimensional growth, respectively), c is the growth index ($c = 0.5$ for diffusion-controlled and $c = 1$ for interface-controlled growth).

It can be seen from Fig. 6 that all the $n(x) - x$ curves exhibit the same tendency that the value of $n(x)$ gradually decreases as the crystallization fraction increases, which means the nucleation rate decreases. For the first and second crystallization processes, the local Avrami exponent begins from $1.5 < n(x) < 2$, which indicates that both of the two crystallization processes are initiated

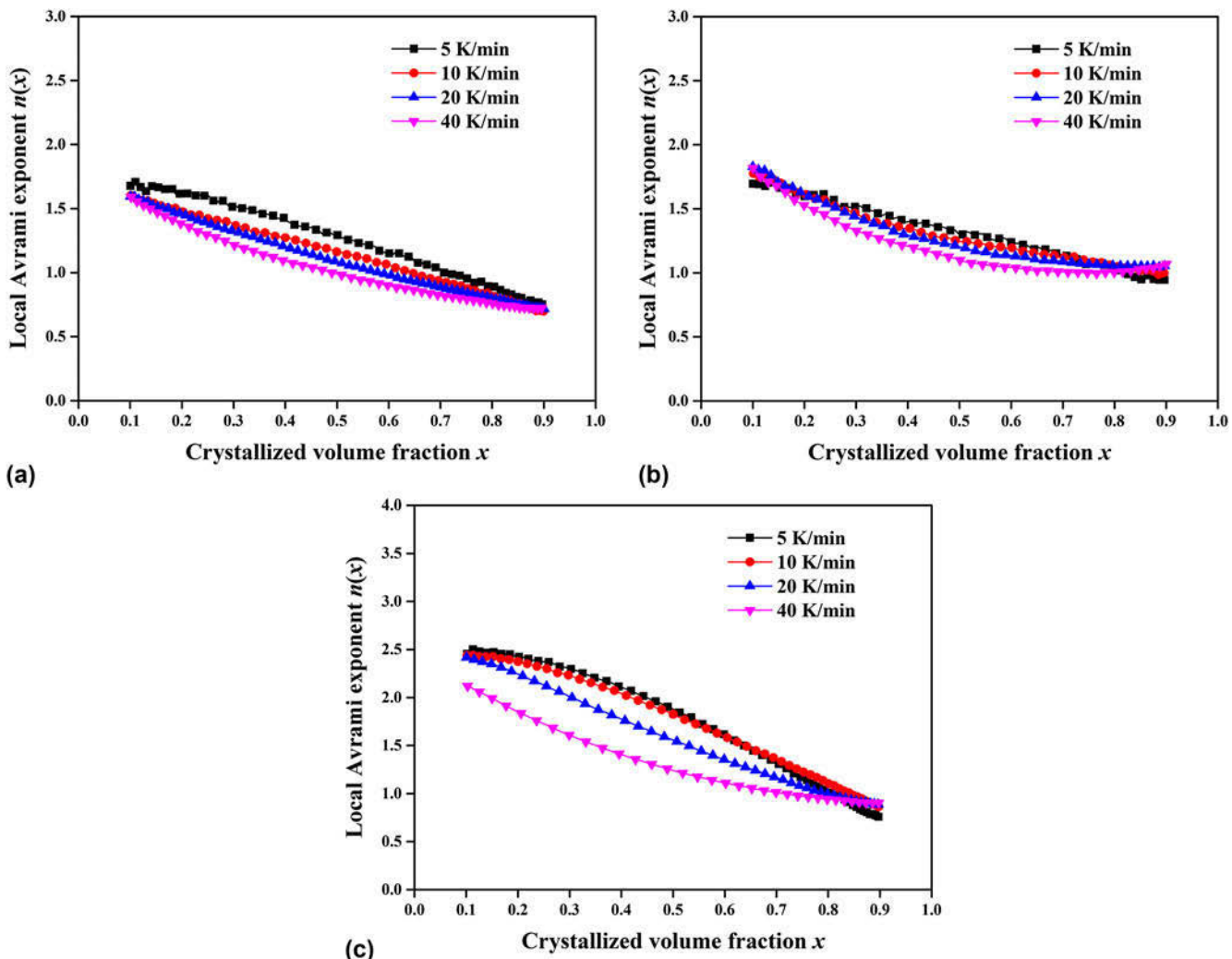


FIG. 6. Variations of the local Avrami exponent versus the crystallized volume fraction x at different heating rates calculated for the $Ti_{20}Zr_{20}Cu_{20}Ni_{20}Be_{20}$ HE-BMG: the (a) first, (b) second, and (c) third exothermic peaks.

by diffusion-controlled one-dimensional growth with a decreasing nucleation rate. As the crystallization proceeds, the local exponent start to decrease and the value of $n(x)$ is below 1.5 in almost the whole crystallization process, indicating that the nucleation is saturated and there are lots of the crystal nuclei growing up directly. For the third crystallization process, the starting value of $n(x)$ is larger than the values of the first and second crystallization processes under the same condition but still smaller than 2.5, and this means that the crystallization mechanism is the growth of primary crystal type and the nucleation rate decreases with time. In the next stage, $n(x)$ also drops below 1.5, indicating that the concentration of pre-existing nuclei has already reached saturation.

S. Cheng et al.¹⁷ have investigated the nonisothermal kinetics of $Zr_{41.2}Ti_{13.8}Cu_{12.5}Ni_{10}Be_{22.5}$ BMG. For the first crystallization event, the local Avrami exponent curves at relatively high heating rates (20 and 40 K/min) increase slowly from ~ 2.0 ($x = 0.1$) to ~ 2.5 ($x = 0.9$), while the

$n(x) - x$ curves at lower heating rates (5 and 10 K/min) decrease first from ~ 2.0 ($x = 0.1$) to the minimum and then increase to ~ 2.5 . The crystallization mechanism of $Zr_{41.2}Ti_{13.8}Cu_{12.5}Ni_{10}Be_{22.5}$ BMG is quite different from that of $Ti_{20}Zr_{20}Cu_{20}Ni_{20}Be_{20}$ HE-BMG.

As the activation energy during the crystallization process is not a constant, Kissinger–Akahira–Sunose (KAS)³⁶ method is used to calculate the local values of activation energy:

$$\ln\left(\frac{\phi}{T(x)^2}\right) = -\frac{E_a(x)}{RT(x)} + d_1 \quad , \quad (6)$$

where $E_a(x)$ and $T(x)$ stand for activation energy and temperature corresponding to the given crystallized volume fraction x ; d_1 is a constant.

Figure 7 shows the KAS plots of the first, second, and third crystallization peaks for $Ti_{20}Zr_{20}Cu_{20}Ni_{20}Be_{20}$

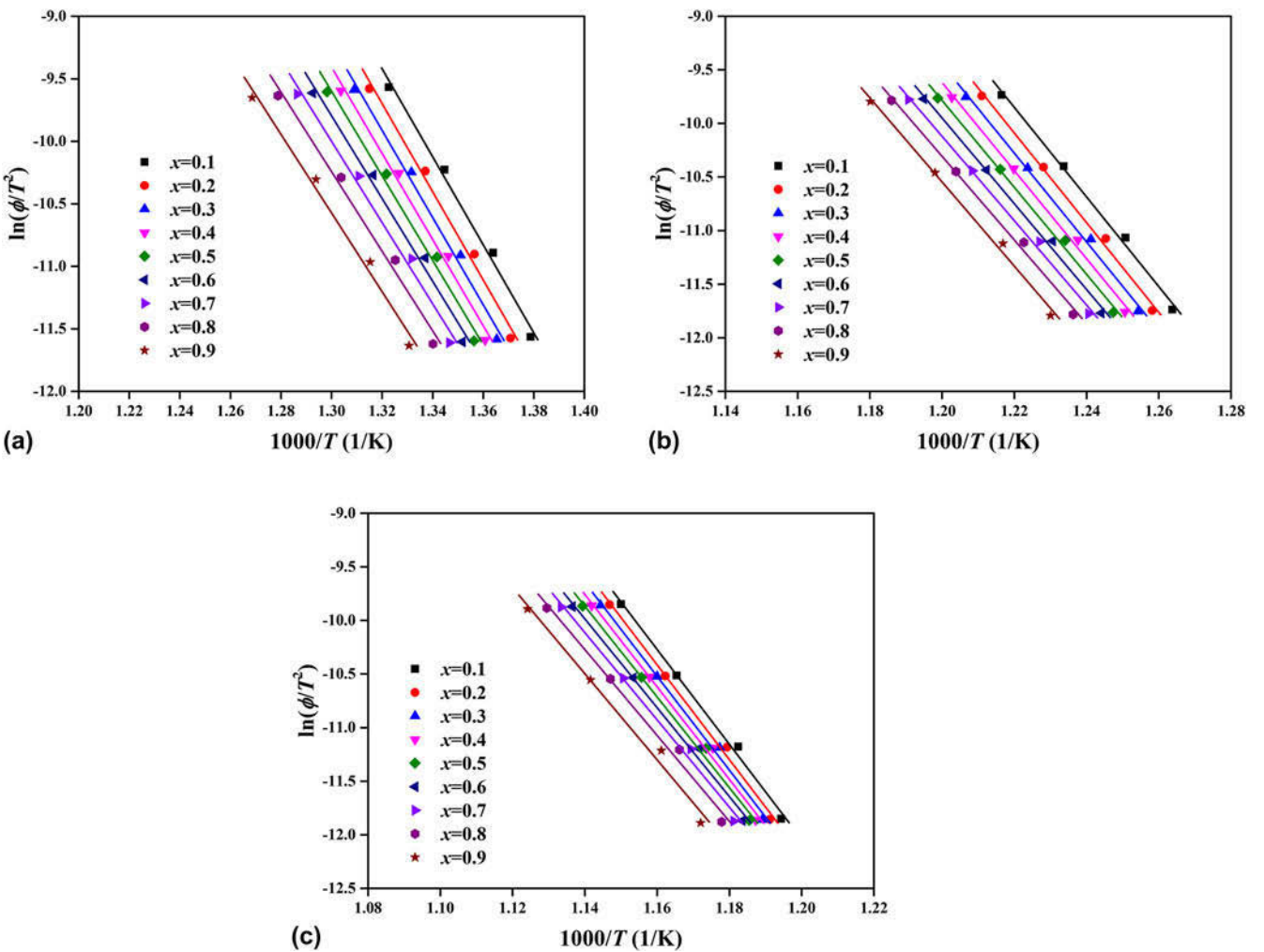


FIG. 7. KAS plots for different crystallization volume fractions x (ranging from 0.1 to 0.9) for the $\text{Ti}_{20}\text{Zr}_{20}\text{Cu}_{20}\text{Ni}_{20}\text{Be}_{20}$ HE-BMG: the (a) first, (b) second, and (c) third exothermic peaks.

HE-BMG. By linear fitting, the evolution of $E_a(x)$ as a function of crystallized volume fraction x (ranging from 0.1 to 0.9) was determined (as shown in Fig. 8). As can be seen, for all the crystallization peaks, the value of $E_a(x)$ is almost stable and can be taken as a constant. The average $E_a(x)$ values for the first, second, and third crystallization peaks are 279.5 ± 14.3 , 336.7 ± 12.3 , and 351.1 ± 15.3 kJ/mol, respectively. In contrast, for $\text{Zr}_{41.2}\text{Ti}_{13.8}\text{Cu}_{12.5}\text{Ni}_{10}\text{Be}_{22.5}$ BMG,¹⁷ the value of $E_a(x)$ for the first crystallization peak increases dramatically from ~ 170 kJ/mol ($x = 0.1$) to ~ 230 kJ/mol ($x = 0.9$), which indicates that the crystallization process of $\text{Zr}_{41.2}\text{Ti}_{13.8}\text{Cu}_{12.5}\text{Ni}_{10}\text{Be}_{22.5}$ BMG is more complex.

C. Kinetic fragility

Kinetic fragility (m) presents the degree of deviations from the Arrhenius law above T_g and is widely used to estimate the thermal stability or glass-forming ability of metallic glass.²⁵ Angell introduced the kinetic fragility

parameter m as a metric for the viscosity behavior of the undercooled liquid around the glass transition temperature.³⁷

$$m = (D^*/\ln 10) \left(T_g^0 / T_g \right) \left(1 - T_g^0 / T_g \right)^{-2} , \quad (7)$$

where D^* is the strength parameter, T_g^0 is the asymptotic value of T_g , which is usually approximated as the onset of the glass transition temperature at the limit of infinitely slow cooling, and T_g is the glass transition temperature at a heating rate of 20 K/min. The variation of T_g with the heating rate ϕ can be fitted by using Vogel–Fulcher–Tammann (VFT) equation³⁸:

$$\ln(\phi) = \ln C - D^* T_g^0 / \left(T_g - T_g^0 \right) , \quad (8)$$

where C is a constant. The values of D^* and T_g^0 can be obtained by fitting the VFT equation from the heating

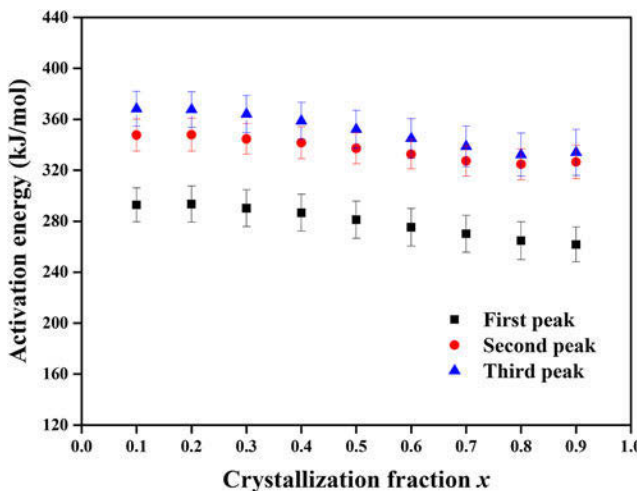


FIG. 8. Dependence of local activation energy $E_a(x)$ on the degree of crystallization volume fraction x .

rate dependence of the glass transition temperature, then the fragility index m can be calculated using Eq. (8).

Figure 9 shows the variation of $\ln \phi$ with T_g fitted by VFT equation for $Ti_{20}Zr_{20}Cu_{20}Ni_{20}Be_{20}$ HE-BMG. The m value of $Ti_{20}Zr_{20}Cu_{20}Ni_{20}Be_{20}$ HE-BMG is calculated to be 23, which is much smaller than those of other BMGs in the same alloy system, such as $Zr_{41.2}Ti_{13.8}Cu_{12.5}Ni_{10}Be_{22.5}$ ($m = 44$) and $Zr_{46.75}Ti_{8.25}Cu_{7.5}Ni_{10}Be_{27.5}$ ($m = 44.2$).¹⁷ Glass forming liquids can be classified into three general categories based on the concept of fragility: strong glass formers ($m < 30$), intermediate glass formers ($30 \leq m < 100$), and fragile glass formers ($m \geq 100$).³⁷ In this sense, the studied $Ti_{20}Zr_{20}Cu_{20}Ni_{20}Be_{20}$ HE-BMG can be classified to the strong glass former. However, it has been perceived that a low m value is not necessarily associated with a superior GFA.^{39–41}

D. Thermodynamics

The Gibbs free energy difference (ΔG) between the supercooled liquid and crystalline states is the driving force of crystallization and plays an important role in predicting the glass-forming ability of multicomponent metallic alloys. The Gibbs energy difference ΔG can be calculated as follows⁴²:

$$\Delta G = \Delta H - T\Delta S , \quad (9)$$

where

$$\Delta H = \Delta H_m - \int_T^{T_m} \Delta C_p^{l-s} dT , \quad (10)$$

and

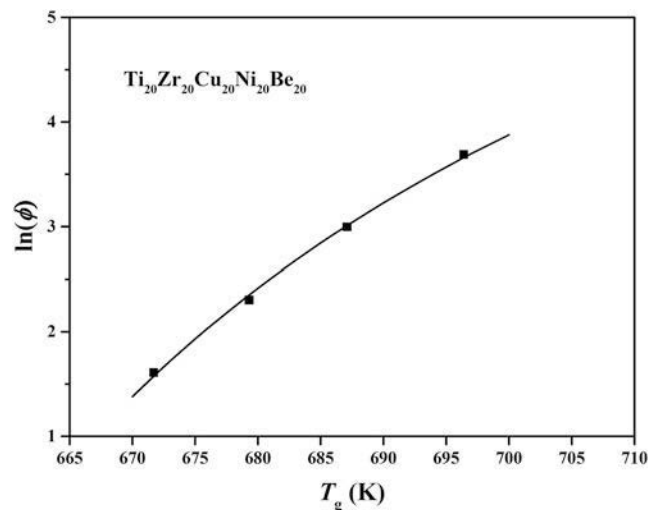


FIG. 9. VFT fit of the $Ti_{20}Zr_{20}Cu_{20}Ni_{20}Be_{20}$ HE-BMG.

$$\Delta S = \Delta S_m - \int_T^{T_m} \Delta C_p^{l-s} \frac{dT}{T} , \quad (11)$$

where T_m is the melting temperature, ΔS_m is the entropy of fusion, and ΔH_m is the enthalpy of fusion. They are related to each other by the following equation:

$$\Delta S_m = \Delta H_m / T_m . \quad (12)$$

Using Eqs. (10)–(12) in Eq. (9), we obtain the following expression for ΔG :

$$\Delta G = \Delta H_m \frac{T_m - T}{T_m} - \int_T^{T_m} \Delta C_p^{l-s} dT + T \int_T^{T_m} \frac{\Delta C_p^{l-s}}{T} dT , \quad (13)$$

where ΔC_p^{l-s} is the heat capacity difference between solid and liquid.

For $Ti_{20}Zr_{20}Cu_{20}Ni_{20}Be_{20}$ HE-BMG, ΔH_m and T_m can be easily obtained by DSC (as shown in Fig. 10). However, it is difficult to measure the heat capacity of the supercooled liquid (C_p^l) accurately. Based on the approximation of ΔC_p^{l-s} , Lad et al.⁴³ got the following equation to calculate ΔG for metallic alloys which have wide supercooled liquid region:

$$\Delta G = \frac{\Delta H_m \Delta T}{T_m} \left(1 - \frac{\Delta T}{2T} \right) , \quad (14)$$

where $\Delta T = T_m - T$.

Figure 11 shows the Gibbs free energy difference as a function of temperature normalized to T_m for $Ti_{20}Zr_{20}Cu_{20}Ni_{20}Be_{20}$ HE-BMG. For comparison, the Gibbs energy difference curve of $Zr_{41.2}Ti_{13.8}Cu_{12.5}Ni_{10}Be_{22.5}$ BMG is also provided.¹⁷ It is found that the value of the

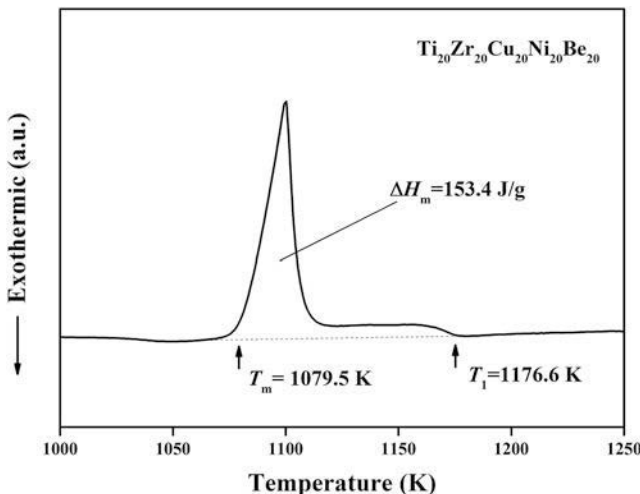


FIG. 10. DSC curve of the $Ti_{20}Zr_{20}Cu_{20}Ni_{20}Be_{20}$ HE-BMG around the melting temperature at a heating rate of 20 K/min.

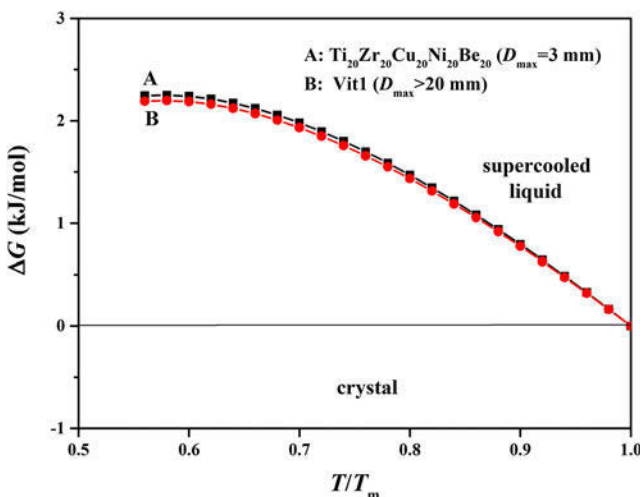


FIG. 11. Gibbs free energy difference curves for $Ti_{20}Zr_{20}Cu_{20}Ni_{20}Be_{20}$ HE-BMG and $Zr_{41.2}Ti_{13.8}Cu_{12.5}Ni_{10}Be_{22.5}$ BMG.

Gibbs energy difference of $Ti_{20}Zr_{20}Cu_{20}Ni_{20}Be_{20}$ HE-BMG is slightly higher than that of $Zr_{41.2}Ti_{13.8}Cu_{12.5}Ni_{10}Be_{22.5}$ BMG. As $Zr_{41.2}Ti_{13.8}Cu_{12.5}Ni_{10}Be_{22.5}$ BMG is a well-known alloy with high glass-forming ability, the Gibbs free energy difference of this alloy is lower than that of most other BMGs.⁴² Correspondingly, $Ti_{20}Zr_{20}Cu_{20}Ni_{20}Be_{20}$ HE-BMG shows relatively low Gibbs free energy difference.

E. Glass-forming ability

In general, the alloys which possess high crystallization activation energy, small fragility index, and low Gibbs energy difference are probably good glass former. Based on the above results, $Ti_{20}Zr_{20}Cu_{20}Ni_{20}Be_{20}$ HE-BMG is expected to have good glass-forming ability by comparison with $Zr_{41.2}Ti_{13.8}Cu_{12.5}Ni_{10}Be_{22.5}$ BMG.

However, $Zr_{41.2}Ti_{13.8}Cu_{12.5}Ni_{10}Be_{22.5}$ BMG also exhibits a wider supercooled liquid region (82 K, heating rate 20 K/min),¹⁷ implying a higher thermal stability. Moreover, the critical size of $Ti_{20}Zr_{20}Cu_{20}Ni_{20}Be_{20}$ HE-BMG is only 3 mm, which is much smaller than that of $Zr_{41.2}Ti_{13.8}Cu_{12.5}Ni_{10}Be_{22.5}$ BMG (over 20 mm).¹⁴

This result can be explained from several aspects. First, by treating Ti–Zr–Cu–Ni–Be alloy system as a pseudo ternary system, it has been found that the good glass forming alloys in this quinary system always locates at the (Ti + Zr)-rich corner (60–65 at.%), while poor in (Cu + Ni), which is less than 25 at.%.¹³ Thus, $Ti_{20}Zr_{20}Cu_{20}Ni_{20}Be_{20}$ alloy deviates from the good glass-forming area. As strong evidence of the above analysis, the liquidus temperature T_1 (also the melting temperature T_m) of $Zr_{41.2}Ti_{13.8}Cu_{12.5}Ni_{10}Be_{22.5}$ BMG (993 K)¹³ is obviously lower than that of $Ti_{20}Zr_{20}Cu_{20}Ni_{20}Be_{20}$ HE-BMG (1176.6 K), resulting in a higher value of T_{rg} (defined as T_g/T_1 , heating rate: 20 K/min, 0.584 for $Ti_{20}Zr_{20}Cu_{20}Ni_{20}Be_{20}$ HE-BMG and 0.629 for $Zr_{41.2}Ti_{13.8}Cu_{12.5}Ni_{10}Be_{22.5}$ BMG). It should be noted that a higher melting point always corresponds to the presence of a higher volume fraction of high melting point phases, which would also well explain why the E_{p1} , E_{p2} , and E_{p3} values are considerably higher than those reported for $Zr_{41.2}Ti_{13.8}Cu_{12.5}Ni_{10}Be_{22.5}$ alloy. Second, from the topological perspective, $Zr_{41.2}Ti_{13.8}Cu_{12.5}Ni_{10}Be_{22.5}$ alloy satisfies ideal efficient atomic-packing conditions, which is beneficial to the glass formation. Third, based on Eq. (9), the high entropy of mixing is beneficial to decrease the Gibbs free energy difference. But meanwhile, according to Adam–Gibbs equation,⁴⁴ the high entropy of mixing also leads to low viscosity and a high mobility of the atoms in the liquid.⁷ So high entropy effect has both advantageous and disadvantageous to the glass-forming ability and the negative effect might play a greater role.

IV. CONCLUSIONS

(1) The crystallization of the $Ti_{20}Zr_{20}Cu_{20}Ni_{20}Be_{20}$ HE-BMG exhibits three steps and the crystallization products are indexed as FCC and BCC solid solutions together with Ni_7Zr_2 intermetallic phase. The apparent activation energies of E_g , E_x , E_{p1} , E_{p2} , and E_{p3} have been estimated by Kissinger equation and Ozawa equation.

(2) The Avrami exponent is less than 1.5 in the whole process of the first and second crystallization events and most cases of the third crystallization event, indicating that the main crystallization mechanism of diffusion-controlled growth of pre-existing nuclei. The local activation energy keeps stable during the whole crystallization process with average values of 279.5 ± 14.3 , 336.7 ± 12.3 , and 351.1 ± 15.3 kJ/mol, respectively, for the first, second, and third crystallization events.

(3) According to the small value of fragility index (23), $Ti_{20}Zr_{20}Cu_{20}Ni_{20}Be_{20}$ HE-BMG can be classified into “strong glasses”. $Ti_{20}Zr_{20}Cu_{20}Ni_{20}Be_{20}$ HE-BMG also exhibits relatively low Gibbs free energy difference.

(4) By comparison with $Zr_{41.2}Ti_{13.8}Cu_{12.5}Ni_{10}Be_{22.5}$ BMG, the larger values of activation energies for crystallization (E_x and E_{p1}), smaller fragility index, and similar Gibbs free energy difference of $Ti_{20}Zr_{20}Cu_{20}Ni_{20}Be_{20}$ HE-BMG do not correspond to the better thermal stability and glass-forming ability. This might be attributed to the deviation of best glass forming region and the low viscosity induced by the high entropy effect.

ACKNOWLEDGMENT

This work was supported by the National Natural Science Foundation of China (Grant Nos. 51271095 and 51101090).

REFERENCES

- J.W. Yeh, S.K. Chen, S.J. Lin, J.Y. Gan, T.S. Chin, T.T. Shun, C.H. Tsau, and S.Y. Chang: Nanostructured high-entropy alloys with multiple principal elements: Novel alloy design concepts and outcomes. *Adv. Eng. Mater.* **6**, 299 (2004).
- O.N. Senkov, G.B. Wilks, D.B. Miracle, C.P. Chuang, and P.K. Liaw: Refractory high-entropy alloys. *Intermetallics* **18**, 1758 (2010).
- Y. Zhang, X. Yang, and P.K. Liaw: Alloy design and properties optimization of high-entropy alloys. *JOM* **64**, 7 (2012).
- W.H. Wang, C. Dong, and C.H. Shek: Bulk metallic glasses. *Mater. Sci. Eng., R* **44**, 45 (2004).
- A. Inoue and A. Takeuchi: Recent development and application products of bulk glassy alloys. *Acta Mater.* **59**, 2243 (2011).
- S. Guo, C. Ng, J. Lu, and C.T. Liu: Effect of valence electron concentration on stability of fcc or bcc phase in high entropy alloys. *J. Appl. Phys.* **109**, 103505 (2011).
- Y. Zhang, Y.J. Zhou, J.P. Lin, G.L. Chen, and P.K. Liaw: Solid-solution phase formation rules for multi-component alloys. *Adv. Eng. Mater.* **10**, 534 (2008).
- K. Zhao, X.X. Xia, H.Y. Bai, D.Q. Zhao, and W.H. Wang: Room temperature homogeneous flow in a bulk metallic glass with low glass transition temperature. *Appl. Phys. Lett.* **98**, 141913 (2011).
- W.H. Wang: High-entropy metallic glasses. *JOM* **66**, 2067 (2014).
- L. Ma, L. Wang, T. Zhang, and A. Inoue: Bulk glass formation of Ti-Zr-Hf-Cu-M (M=Fe, Co, Ni) alloys. *Mater. Trans.* **43**, 277 (2002).
- X.Q. Gao, K. Zhao, H.B. Ke, D.W. Ding, W.H. Wang, and H.Y. Bai: High mixing entropy bulk metallic glasses. *J. Non-Cryst. Solids* **357**, 3557 (2011).
- A. Takeuchi, N. Chen, T. Wada, Y. Yokoyama, H. Kato, A. Inoue, and J.W. Yeh: $Pd_{20}Pt_{20}Cu_{20}Ni_{20}P_{20}$ high-entropy alloy as a bulk metallic glass in the centimeter. *Intermetallics* **19**, 1546 (2011).
- H.Y. Ding and K.F. Yao: High entropy $Ti_{20}Zr_{20}Cu_{20}Ni_{20}Be_{20}$ bulk metallic glass. *J. Non-Cryst. Solids* **364**, 9 (2013).
- A. Peker and W.L. Johnson: A highly processable metallic glass: $Zr_{41.2}Ti_{13.8}Cu_{12.5}Ni_{10.0}Be_{22.5}$. *Appl. Phys. Lett.* **63**, 2342 (1993).
- C.C. Hays, C.P. Kim, and W.L. Johnson: Large supercooled liquid region and phase separation in the Zr-Ti-Ni-Cu-Be bulk metallic glasses. *Appl. Phys. Lett.* **75**, 1089 (1999).
- Y.C. Kim, W.T. Kim, and D.H. Kim: A development of Ti-based bulk metallic glass. *Mater. Sci. Eng., A* **375–377**, 127 (2004).
- S. Cheng, C. Wang, M. Ma, D. Shan, and B. Guo: Non-isothermal crystallization kinetics of $Zr_{41.2}Ti_{13.8}Cu_{12.5}Ni_{10}Be_{22.5}$ amorphous alloy. *Thermochim. Acta* **587**, 11 (2014).
- P. Gong, S.F. Zhao, X. Wang, and K.F. Yao: Non-isothermal crystallization kinetics and glass-forming ability of $Ti_{41}Zr_{25}Be_{25}Fe_6$ bulk metallic glass investigated by differential scanning calorimetry. *Appl. Phys. A* **120**, 145 (2015).
- K.K. Song, P. Gargarella, S. Pauly, G.Z. Ma, U. Kuhn, and J. Eckert: Correlation between glass-forming ability, thermal stability, and crystallization kinetics of Cu-Zr-Ag metallic glasses. *J. Appl. Phys.* **112**, 063503 (2012).
- K.G. Raval, K.N. Lad, A. Pratap, A.M. Awasthi, and S. Bhardwaj: Crystallization kinetics of a multicomponent Fe-based amorphous alloy using modulated differential scanning calorimetry. *Thermochim. Acta* **425**, 47 (2005).
- Y.D. Sun, P. Shen, Z.Q. Li, J.S. Liu, M.Q. Cong, and M. Jiang: Kinetics of crystallization process of Mg-Cu-Gd based bulk metallic glasses. *J. Non-Cryst. Solids* **358**, 1120 (2012).
- F.X. Qin, H.F. Zhang, B.Z. Ding, and Z.Q. Hu: Nanocrystallization kinetics of Ni-based bulk amorphous alloy. *Intermetallics* **12**, 1197 (2004).
- L. Hu and F. Ye: Crystallization kinetics of $Ca_{65}Mg_{15}Zn_{20}$ bulk metallic glass. *J. Alloys Compd.* **557**, 160 (2013).
- S.F. Chen, C.Y. Chen, and C.H. Lin: Insight on the glass-forming ability of Al-Y-Ni-Ce bulk metallic glass. *J. Alloys Compd.* **637**, 418 (2015).
- J.C. Qiao, J.M. Pelletier, Q. Wang, W. Jiao, and W.H. Wang: On calorimetric study of the fragility in bulk metallic glasses with low glass transition temperature: $(Ce_{0.72}Cu_{0.28})_{90-x}Al10Fe_x$ ($x=0, 5$ or 10) and $Zn_{38}Mg_{12}Ca_{32}Yb_{18}$. *Intermetallics* **19**, 1367 (2011).
- Y.C. Kim, J.M. Park, J.K. Lee, D.H. Bae, W.T. Kim, and D.H. Kim: Amorphous and icosahedral phases in Ti-Zr-Cu-Ni-be alloys. *Mater. Sci. Eng., A* **375–377**, 749 (2004).
- S.B. Qiu, K.F. Yao, and P. Gong: Effects of crystallization fractions on mechanical properties of Zr-based metallic glass matrix composites. *Sci. China: Phys., Mech. Astron.* **53**, 424 (2010).
- K.B. Kim, Y. Zhang, P.J. Warren, and B. Cantor: Crystallization behavior in a new multicomponent $Ti_{16.6}Zr_{16.6}Hf_{16.6}Ni_{20}Cu_{20}Al_{10}$ metallic glass developed by the equiatomic substitution technique. *Philos. Mag.* **83**, 2371 (2003).
- W. Zhou, J. Hou, Z. Zhong, and J. Li: Effect of Ag content on thermal stability and crystallization behavior of Zr-Cu-Ni-Al-Ag bulk metallic glass. *J. Non-Cryst. Solids* **411**, 132 (2015).
- H.E. Kissinger: Reaction kinetics in differential thermal analysis. *Anal. Chem.* **29**, 1702 (1957).
- T. Ozawa: Kinetic analysis of derivative curves in thermal analysis. *J. Therm. Anal. Calorim.* **2**, 301 (1970).
- N. Chen, Y. Li, and K.F. Yao: Thermal stability and fragility of Pd-Si binary bulk metallic glasses. *J. Alloys Compd.* **504**, S211 (2010).
- J. Málek: The applicability of Johnson-Mehl-Avrami model in the thermal analysis of the crystallization kinetics of glasses. *Thermochim. Acta* **267**, 61 (1995).
- J.S. Blázquez, C.F. Conde, and A. Conde: Non-isothermal approach to isokinetic crystallization processes: Application to the nanocrystallization of HITPERM alloys. *Acta Mater.* **53**, 2305 (2005).
- S. Ranganathan and M. Von Heimendahl: The three activation energies with isothermal transformations: Applications to metallic glasses. *J. Mater. Sci.* **16**, 2401 (1981).
- A.T. Patel and A. Pratap: Kinetics of crystallization of $Zr_{52}Cu_{18}Ni_{14}Al_{10}Ti_6$ metallic glass. *J. Therm. Anal. Calorim.* **107**, 159 (2012).
- C.A. Angell: Formation of glasses from liquids and biopolymers. *Science* **267**, 1924 (1995).

38. R. Brüning and K. Samwer: Glass transition on long time scales. *Phys. Rev. B* **46**, 11318 (1992).
39. O.N. Senkov: Correlation between fragility and glass-forming ability of metallic alloys. *Phys. Rev. B* **76**, 104202 (2007).
40. E.S. Park, J.H. Na, and D.H. Kim: Correlation between fragility and glass-forming ability/plasticity in metallic glass-forming alloy. *Appl. Phys. Lett.* **91**, 031907 (2007).
41. C. Chattopadhyay, S. Sangal, and K. Mondal: Relook on fitting of viscosity with undercooling of glassy liquids. *Bull. Mater. Sci.* **37**, 83 (2014).
42. R. Busch, Y.J. Kim, and W.L. Johnson: Thermodynamics and kinetics of the undercooled liquid and the glass transition of the $Zr_{41.2}Ti_{13.8}Cu_{12.5}Ni_{10.0}Be_{22.5}$ alloy. *J. Appl. Phys.* **77**, 4039 (1995).
43. K.N. Lad, K.G. Raval, and A. Pratap: Estimation of Gibbs free energy difference in bulk metallic glass forming alloys. *J. Non-Cryst. Solids* **334–335**, 259 (2004).
44. G. Adam and J.H. Gibbs: On the temperature dependence of cooperative relaxation properties in glass-forming liquids. *J. Chem. Phys.* **43**, 139 (1965).